Contrail Detection and Coverage Estimation across Air Route Traffic Control Centers from Satellite Observations

Rong Tang[a], Kam K.H. Ng[a, b*]
[a]Department of Aeronautical and Aviation Engineering
[b]Research Institute for Sustainable Urban Development
The Hong Kong Polytechnic University
Hung Hom, Hong Kong SAR
rong258.tang@connect.polyu.hk, kam.kh.ng@polyu.edu.hk

Yutong Chen
Air Traffic Management Research Institute
Nanyang Technological University
Singapore
yutong.chen@ntu.edu.sg

Yan Xu
School of Electronics and Information Engineering
Beihang University
Beijing, China
yan.xu@buaa.edu.cn

***Abstract*—Contrails are recognised as a net warming contributor to aviation-induced climate impact, and their detection from satellite imagery provides an observational basis for estimating coverage and informing rerouting strategies. While informative, continental-scale estimates are insufficient for operational use, being constrained by air traffic management complexity and costs from CO_2/non-CO_2 trade-offs. A more feasible approach is to identify contrail-intense air traffic control regions and corridors, where targeted rerouting could deliver greater climate benefit at lower operational cost. We propose a joint spatial–frequency loss that conditions learning to emphasise contrail samples while capturing their line-shaped structures. On the OpenContrails dataset [1], our method consistently improves detection across multiple binarisation thresholds, achieving a global dice score of 70.23%. The proposed method is applied to GOES-16 imagery to estimate contrail coverage over CONUS and at the scale of individual Air Route Traffic Control Centers (ARTCCs). Multi-threshold analysis yields a range of contrail coverage from 0.015% to 0.254%, with a moderate average of 0.115% across 60 days in 2024. The moderate estimate reveals clear seasonal cycles, with greater contrail occurrence in winter and spring, and diurnal peaks between 08:00 and 10:00 local time across most regions. Joint evaluation with meteorological conditions further identifies contrail-intense zones and corridors, implying an uneven potential for region-specific contrail mitigation due to notable anomalies between ARTCCs.**

***Keywords*—Aviation sustainability, Non-CO_2 effects, Contrail coverage, Remote sensing, Deep learning**

I. Introduction

Compared with sustainable aviation fuel and next-generation propulsion, air traffic flow management (ATFM) could offer an instant potential for mitigating short-lived contrails through tactical rerouting [2], [3]. For example, [4] showed that only 2.2% of flights accounted for 80% of contrail energy forcing, and that rerouting just 1.7% of the fleet could reduce this forcing by up to 59.3% in the target region. Such strategies have also been tested in real-world operations [5], confirming contrail reduction based on satellite observations of outbound and return flights. Nonetheless, large-scale deployment remains challenging: intense contrail formation typically occurs within narrow temporal and spatial windows, limiting the probability for beneficial planning, while the trade-offs (CO_2/non-CO_2) in aviation emissions, traffic complexity, airspace capacity, and forecast uncertainties further constrain the feasibility [6], [7]. Therefore, detecting contrails in satellite observations and identifying contrail-intense zones (CIZs) provides a direct view of historical contrail coverage, guiding priorities for future mitigation.

Contrail detection and coverage estimation have traditionally relied on microphysical formation models governed by the Schmidt–Appleman criterion (SAc) [8], combined with filtering of ice supersaturated regions and plume-chemistry simulations such as CoCiP and APCEMM [9]. While these approaches, often driven by reanalysis meteorology and ADS-B data [10], [11], enable large-scale assessments, they suffer from substantial biases due to uncertainties in upper-tropospheric and lower-stratospheric conditions at cruise altitudes [12].

Recent advances in deep learning–based semantic segmentation [13], [14] allow direct visual detection of contrails from satellite imagery, improving accuracy and reducing meteorological dependency. Such observation-driven approaches provide a more reliable basis for identifying when and where persistent contrails occur, complementing physics-based simulations and supporting contrail-mitigation strategies in air traffic flow management [4], [15], [16]. To inform climate-oriented flight planning effectively, however, contrail coverage must be resolved not only in time but also across operational regions. Existing assessments have mostly focused on broad domains to capture general patterns of contrail coverage [17]–[19]. Yet, inter-regional variations in air traffic complexity

and meteorology necessitate finer, region-specific analyses to support actionable, dynamic contrail avoidance.

To this end, this work explicitly accounts for line-shaped contrails in developing a deep learning-based detection model, which is subsequently employed to examine contrail coverage across air traffic control regions. The identified seasonal and diurnal patterns, along with regional anomalies linked to meteorology, are analysed to inform targeted and effective flight rerouting strategies. In summary, the core contributions of this work include:

1) Introducing a joint spatial-frequency loss leveraging the Discrete Fourier Transform (DFT) to enhance contrail detection, achieving state-of-the-art performance on the OpenContrails dataset [1] while seamlessly integrating into end-to-end segmentation models with negligible computational overhead;
2) Estimating high-temporal-resolution contrail coverage across CONUS, down to individual Air Route Traffic Control Centers (ARTCCs), revealing CIZs along metropolitan clusters and connecting corridors over 60 days of GOES-16 observations [20].

The paper is organised as follows. The used data sources are introduced in Section II. Section III describes joint spatial-frequency loss and multi-level evaluations. In Section IV, comparative analyses are presented to highlight the spatio-temporal variations of contrail coverage over CONUS and each ARTCC. Finally, Section V gives the implications and limitations of this work, followed by the conclusion and potential future extensions in Section VI.

II. Data

Our deep-learning segmentation models were trained on OpenContrails, a human-labelled and pixel-level-distributed contrail dataset from the GOES-16 [20], widely used in contrail detection research [1]. Below, we briefly describe the additional data and their preparation for our case study.

A. GOES-16 CONUS Disk

This work processed 60 days of satellite records (the first half of January, April, July, and October 2024) from the GOES-16 CONUS disk, which scans the CONUS region every 5 minutes, compared with 10–15 minutes for the full disk depending on the scan mode [20], for seasonal contrail coverage estimation. Each satellite scan is divided into 60 patches with a horizontal dimension of 250×250 pixels, resulting in approximately one million patches after excluding the four upper-left patches due to large view angles. Each patch is padded to 256×256 pixels and then processed by the segmentation model to generate pixel-level contrail masks.

B. Meteorology and Air Traffic Flow

In our case study, the temperature and relative humidity data used in our analysis are obtained from the fifth generation of ECMWF reanalysis (ERA5) pressure-level products [21]. Seven pressure levels (400, 350, 300, 250, 225, 200, and 175 hPa) are included ($0.25° \times 0.25°$ spatial and 1 h temporal resolution), corresponding approximately to geopotential altitudes of 7.2 to 12.6 km, thereby covering typical enroute flight levels. The source trajectories, obtained from ADS-B records, are accessed from OpenSky [22], [23] and clipped to altitudes above 7.2 km.

III. Contrail Detection

To enhance alignment between detected contrails and ground truth, we incorporate a joint spatial-frequency loss. For active samples (containing at least one contrail pixel), the distance in frequency space is calculated in parallel with the conventional spatial loss using the DFT, enabling fast transformation and end-to-end gradient propagation. This frequency term acts as a regularisation, emphasising positive pixels and conditionally constraining model–ground truth alignment.

A. Joint Spatial-Frequency Loss

Since contrail-free samples have masks of all zeros, yielding identical frequency features, the frequency-concerned loss is computed only for active samples containing at least one contrail pixel. For a batch of N samples $(Y_i, \hat{Y}_i)$, where Y_i and $\hat{Y}_i$ are the ground truth and detected contrail probability maps, respectively, the L1-based frequency distance (FD) over $n, n \in [1, N]$ active samples, is formulated as

$$\mathcal{L}_{FD}(Y, \hat{Y}) = \frac{1}{n} \sum_{i=1}^{n} \left\| \mathcal{F}(Y_i) - \mathcal{F}(\hat{Y}_i) \right\|_1, \tag{1}$$

where $\mathcal{F}(*)$ is a 2D DFT to transform spatial features into the frequency domain.

This loss focuses the model on the alignment of ground truth and detection in the frequency domain, enhancing the learning of line-shaped contrail structures. The FD loss also effectively acts as an implicit weighting mechanism, focusing more on positive contrail pixels against a large background. Combined with the conventional spatial loss $\mathcal{L}_{\text{base}}$ (e.g., binary cross-entropy (BCE)), the joint spatial-frequency loss is defined as

$$\mathcal{L}_{\text{joint}}(Y, \hat{Y}) = (1 - \lambda)\mathcal{L}_{\text{base}}(Y, \hat{Y}) + \lambda \mathcal{L}_{FD}(Y, \hat{Y}), \tag{2}$$

where the weight λ is used to adjust the relative contributions of the two loss components, and is set as 0.9, where $\mathcal{L}_{FD}$ improves the overall performance based on sensitivity analysis.

B. Model and Training

1) UNet_MaxViT-tiny: In this work, we employ a state-of-the-art contrail detection model proposed in [14]. The model integrates the MaxViT-tiny module as an encoder within a UNet architecture to enable efficient yet low-cost contrail detection [13], [24]. MaxViT-tiny is based on a multi-axis attention mechanism, employing interlaced window attention and grid attention to capture both local and global receptive fields across the image, while maintaining lower computational complexity compared to standard self-attention. A subsequent study proposed combining UNet++ with CoAtNet to achieve modest performance improvements, but at a substantially higher computational cost [25]. Consequently, the relatively lightweight yet effective UNet_MaxViT-tiny architecture is selected to process the large volume of image patches efficiently.

2) Implementation: The UNet_MaxViT-tiny model is implemented using PyTorch and the segmentation models repository [26], and it is trained and evaluated on a single NVIDIA L40 GPU. The detailed model training configurations are as follows:

- The batch size is set to 8 due to memory constraints when resizing images to 512×512, with training conducted over 40 epochs, as suggested in [14].
- The initial learning rate is 8.0×10^{-4}, gradually decaying to 1.0×10^{-6} over a half-cycle cosine schedule. A linear warm-up from 1.0×10^{8} to 8.0×10^{-4} over the first 500 training steps is applied to stabilise the training process.
- The AdamW optimiser is applied with a weight decay of 0.01 [27]. The base loss function BCE ($\mathcal{L}_{\text{base}} = \mathcal{L}_{\text{bce}}$) incorporates the **pixel-shift design** from [14], which markedly enhances contrail detection performance on Opencontrails.
- Detailed data augmentation procedures and hyperparameter optimisation strategies can be found in [14], [25].

C. Multi-level Evaluation

1) Evaluation Metrics: Given a confusion matrix comprising true positives (TP), false positives (FP), false negatives (FN), and true negatives (TN), the global dice score and the intersection over union (IoU) are employed to quantify the overlap between the identified region and the ground truth [25]. Considering that most samples contain less than 2.5% valid pixels in the OpenContrails dataset, using global metrics rather than sample-averaged counterparts provides a more comprehensive evaluation of contrail detection performance. The global dice score is defined as:

$$\text{Dice} = \frac{2\times(Y\cap\hat{Y})}{|Y|+|\hat{Y}|} = \frac{2\times\text{TP}}{2\times\text{TP}+\text{FP}+\text{FN}}, \tag{3}$$

where Y and $\hat{Y}$ denote the ground truth and the detected contrail labels at a pixel level, respectively. Similarly, the IoU is expressed as:

$$\text{IoU} = \frac{Y\cap\hat{Y}}{|Y|\cup|\hat{Y}|} = \frac{\text{TP}}{\text{TP + FP + FN}}. \tag{4}$$

In addition to the global dice and IoU scores, the recall and precision of contrail detection are also considered, providing reference metrics for the proportion of missed and falsely detected contrail pixels from a conventional binary classification perspective.

2) Results: A 4-fold cross-validation randomly splits the training and validation data from the released "training" subset. Quantitative results are evaluated on the released "validation" subset and reported as a 4-fold ensemble, averaging quantifications from the four models [25]. The estimated probabilities are binarised using thresholds sampled from 0 to 1 at 0.05 intervals, with the highest global dice score at 0.3. Table I summarises these three levels of quantification.

Without adding trainable parameters or reducing inference speed considerably, training with the designed $\mathcal{L}_{\text{joint}}$ substantially improved evaluation metrics across most binarisation thresholds. Specifically, it enhances the global dice score to 70.23%. Setting the threshold at the optimal dice score yields a balanced performance, with both recall and precision at approximately 70%. Due to the equivalence of dice and F1 scores, this threshold optimises overall performance. Estimates of contrail coverage in the next section are conducted under three threshold scenarios.

TABLE I. ENSEMBLE QUANTIFICATION OF CONTRAIL DETECTION ON THE OPENCONTRAILS DATASET, EXPRESSED AS PERCENTAGES, FOR DIFFERENT BINARIZATION THRESHOLDS. THE BEST RESULTS ARE HIGHLIGHTED IN **BOLD**.

Loss	Threshold	Dice (%)	IoU (%)	Recall (%)	Precision (%)
$\mathcal{L}_{\text{bce}}$	0.05	57.18	40.01	89.36	42.02
	0.30	69.62	53.39	70.19	69.05
	0.95	25.11	14.36	14.42	96.90
$\mathcal{L}_{\text{joint}}$	0.05	57.50	40.35	**89.85**	42.27
	0.30	**70.23**	**54.12**	70.58	69.89
	0.95	23.18	13.11	13.16	**97.13**

IV. CONTRAIL COVERAGE ESTIMATION

Using the spatial-frequency-regularised contrail detection model, contrail coverage is estimated over CONUS and each ARTCC across 60 days in 2024, with 15 consecutive days (1st–15th) selected from January, April, July, and October to represent each season. To facilitate consistent quantification of contrail coverage within a given spatio-temporal window, we define the averaged contrail coverage ratio (ACCR), derived directly from the binarised pixel-wise contrail masks of individual frames. This metric enables high-frequency contrail coverage estimation and supports the analysis of cyclic variations by aggregating chronological sequences of geostationary satellite observations.

A. Averaged Contrail Coverage Ratio

In the proposed pipeline, each satellite frame is processed patch by patch through the contrail detection model to generate a pixel-level contrail mask. We then define the *Contrail Coverage Count*, denoted as $\mathbf{C}^3 := \left(\mathrm{c}^3_{i,j}\right)_{M\times N}$, which represents the pixel-wise accumulation of contrail detections over a given time window. Formally, we have:

$$\mathrm{c}^3_{i,j} = \begin{cases} 0, & \text{contrail-free,} \\ c_{i,j}, & \text{otherwise,} \quad 1 \le c_{i,j} \le C, \end{cases} \tag{5}$$

where $M\times N$ denotes the spatial dimensions of each satellite frame, and $c_{i,j}$ is the number of contrail-positive frames at pixel (i,j) within the specified time window. For an hourly aggregation, $C = 12$ since GOES-16 provides one CONUS frame every 5 minutes. The field $\mathbf{C}^3$ can further be expressed in terms of total covering time by multiplying by 5 minutes.

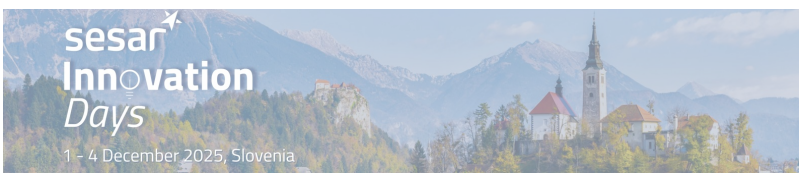

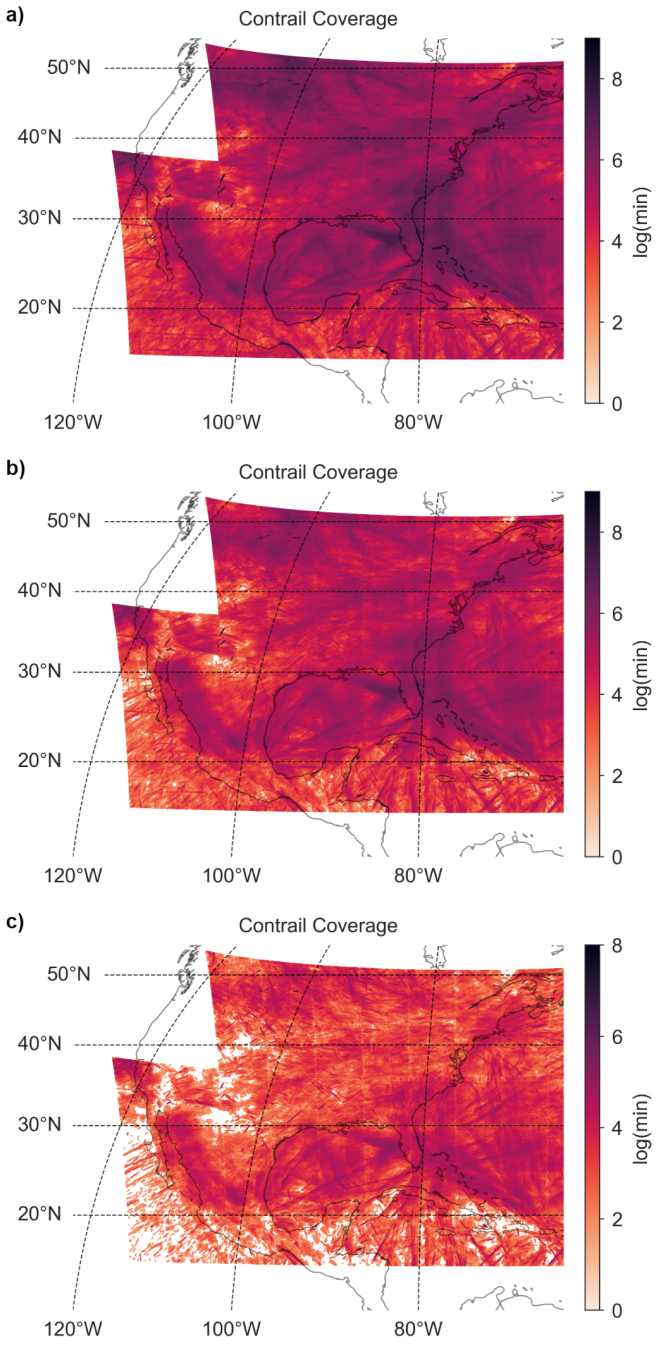

Figure 1. Contrail coverage over CONUS, estimated using thresholds of 0.05 (a), 0.30 (b), and 0.95 (c), with colours representing the logarithm of the averaged daily contrail covering time.

To estimate the overall contrail coverage level, $\mathbf{C}^3$ is then converted to the index ACCR, representing the geo-spatial occurrence of contrails:

$$\mathrm{ACCR} = \frac{\sum \mathbb{I}(\mathbf{C}^3 \geq 1)}{M \times N} \times 100\%, \tag{6}$$

where $\mathbb{I}(\cdot)$ is the indicator function.

TABLE II. COMPARISON OF DAY-AVERAGED CONTRAIL COVERAGE (%) ACROSS CONUS OVER 60 DAYS IN 2024 UNDER DIFFERENT BINARISATION THRESHOLDS.

Threshold	Percentile				
	0th	25th	50th	75th	100th
0.05	0.051	0.117	0.254	0.301	1.017
0.30	0.022	0.055	0.115	0.146	0.471
0.95	0.003	0.008	0.015	0.021	0.058

B. Multi-level Estimations

Before analysing the spatio-temporal variations of contrail coverage across ARTCCs, we first examine how different binarisation thresholds affect the distribution and magnitude of contrail coverage. Owing to the relatively large bias of current deep learning-based contrail detection models on the OpenContrails dataset, it is essential to account for possible underestimation at low thresholds (e.g., 0.05) and overestimation at high thresholds (e.g., 0.95), rather than exploring solely on an intermediate, harmonised threshold such as that optimised for the dice score.

Fig. 1 shows the contrail coverage over the selected 60 days (15 days per season) in 2024 across CONUS, at three binarisation thresholds. To avoid large viewing-angle distortion and incomplete patches, the upper-left 500×500-pixel region of the GOES-16 CONUS frame is excluded from analysis. This area can be supplemented with GOES-18 data in future work.

All subplots are coloured by the logarithm of the daily contrail covering time, averaged over 60 days. Comparing subplots (a) and (c) highlights a substantial difference between under- and overestimation, while the overall geo-distributions and distinct CIZs across CONUS remain consistent. As expected, the moderate estimation lies between the extremes of under- and overestimation, both visually in Fig. 1 and in the day-averaged contrail coverage values in Table II. The moderate estimation, using a threshold of 0.3, generally approximates the midpoint between the estimations from thresholds 0.05 and 0.95.

The moderate estimate is also generally consistent with previous studies using satellite imagery, particularly those from geostationary satellites such as the GOES and the Meteosat Second Generation (MSG) series. For instance, [18] estimated that approximately 0.17% of CONUS was covered by contrails observed from GOES-16, averaged between 2018 and 2019. In the North Atlantic, linear contrails were estimated to cover 0.10%–0.15% of the domain from February 2004 to January 2012 [17], using the Spinning Enhanced Visible and Infra-Red Imager (SEVIRI) onboard the MSG satellites. Meanwhile, [28] found that contrails spatially covered up to 0.085% of the monitored area in central and western Europe in 2016. These findings suggest that linear contrails currently block roughly 0.1%–0.2% of airspace in aviation-active regions, such as CONUS and Europe, under moderate conditions. However,

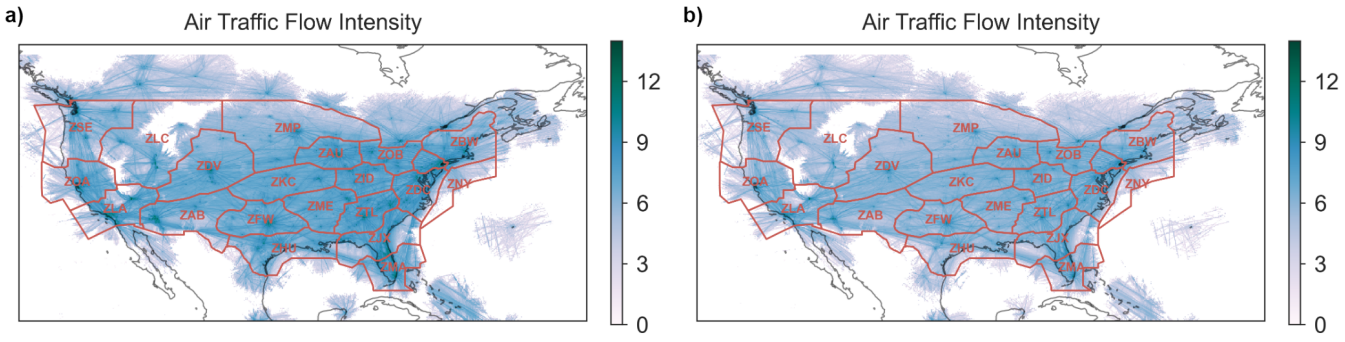

Figure 2. Air traffic flow intensity across CONUS for daytime (07:00–18:00 CST) (a) and nighttime (b), estimated over 8 days in 2024, with colours representing the logarithm of the gridded waypoint histogram at 0.1-degree resolution.

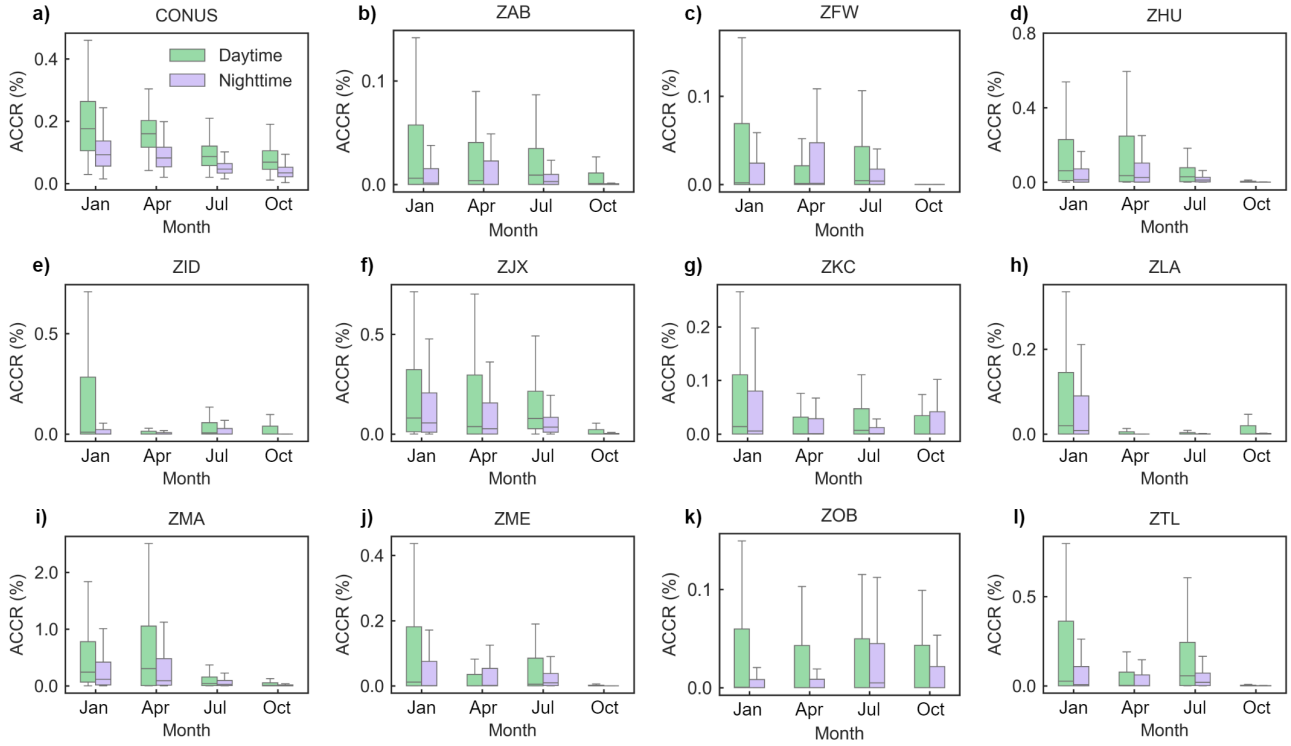

Figure 3. Seasonal ACCR over CONUS and the ARTCCs exhibiting similar patterns in 2024.

this does not apply uniformly to all regions, as explored in the next subsection.

C. Contrail Coverage across ARTCCs

The detected CIZs are concentrated around major airport hubs and extend along connecting air corridors. For example, the Western coast, Florida, and the Northeastern US show dense en-route traffic due to strong metropolitan links. Fig. 2 depicts accumulated traffic flow intensity (count) above 7.2 km over 2 days per season. A high-level network connecting metropolitan clusters is evident, aligning with the intense contrail regions in Fig. 1. Although spatial patterns remain stable from day (07:00–18:00 in Central Standard Time (CST)) to night, flow intensity decreases, explaining the observed diurnal contrail coverage variation. To evaluate mitigation potential, seasonal, diurnal, and spatial distributions are compared across 17 ARTCCs, excluding centers ZSE, ZOA, and ZLC due to excessive filtered-out pixels.

1) Seasonal Patterns: Using the defined ACCR index, Fig. 3(a) illustrates the seasonal patterns of contrail coverage over CONUS and the corresponding values for individual ARTCCs. Winter and spring, represented by the first halves of January and April, exhibit substantially higher contrail coverage over CONUS in 2024 compared to the other seasons. Similar seasonal patterns have been reported in previous studies [18], [29]. When ACCR values are grouped by ARTCCs, many regions follow the general trend of peak contrail coverage in winter, declining towards October, as shown in subplots

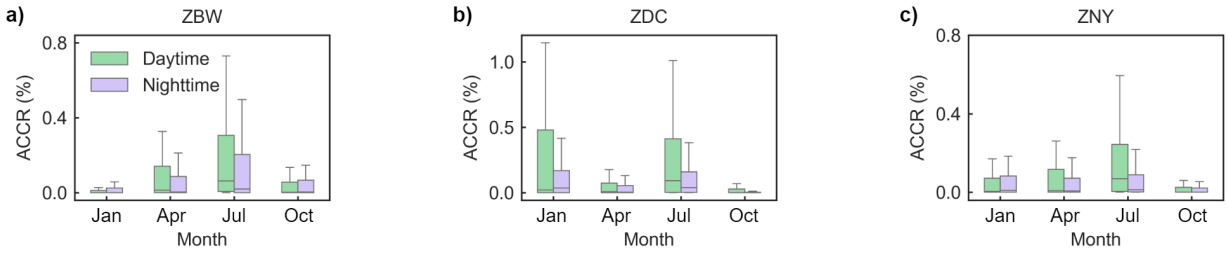

Figure 4. Representative ARTCCs with abnormal ACCR in **July**, compared to the mainstream trend in 2024.

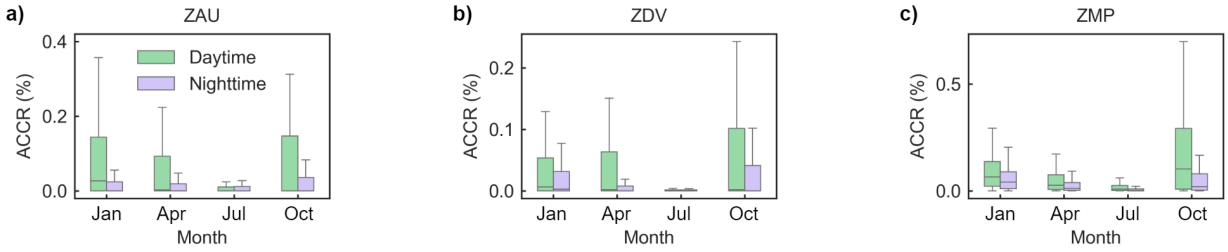

Figure 5. Representative ARTCCs with abnormal ACCR in **October**, compared to the mainstream trend in 2024.

(b)–(l) of Fig. 3. Overall, a decreasing trend from colder to warmer seasons is evident.

By contrast, certain regions exhibit anomalously high contrail coverage in July or October. For instance, subgraph (k) of Fig. 3 shows that ZOB, located in the northern part of the detected area (see Fig. 1), displays such behaviour. Regions with elevated contrail coverage in July are concentrated along the north-eastern coast of CONUS, as illustrated in Fig. 4, whereas those with high contrail coverage in October are found over relatively high-altitude, landlocked areas within CONUS, as exemplified in Fig. 5. In addition, ACCR varied substantially across ARTCCs. For example, approximately 0.3% of the ZMA region (Fig. 3(i)) was covered by contrails in early January and April 2024, compared to less than 0.01% in ZAB (Fig. 3(b)) over the same period. These interregional differences reflect the interplay between meteorological conditions and air traffic in the UTLS.

To explain the findings, ZAB and ZMA are first taken as cases of extremely low and high CCs, respectively. Based on the simplified SAc (temperature $\leq$ 235 K and relative humidity $\geq$ 80%) [30], [31], the contrail-sensitive potential during the evaluation period was assessed using the minimum relative humidity and maximum temperature across flight levels between 7.2 km and 12.6 km, representing the most conservative conditions for contrail formation. Figure 6 shows the resulting temperature and humidity distributions, averaged hourly across pressure levels and grids within CONUS, ZAB, and ZMA. ZAB experienced warmer, drier UTLS conditions, to some extent suppressing contrail formation [8], whereas ZMA was marked by cooler, more humid conditions conducive to contrail formation.

Similarly, for the anomalous July and October in ZNY and ZMP, respectively, Fig. 7 shows their temperature and relative

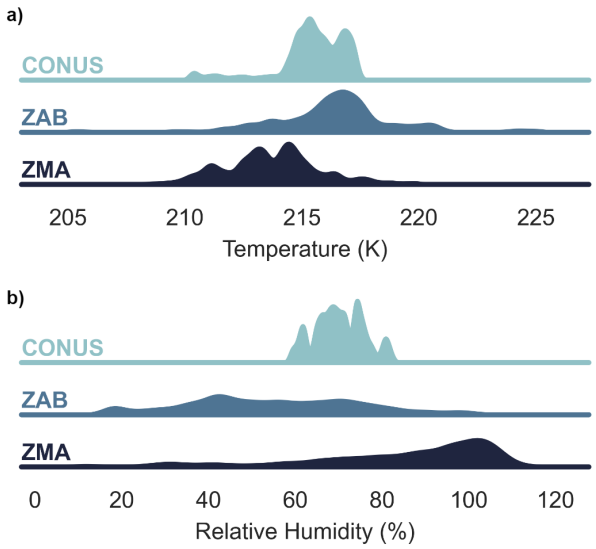

Figure 6. Distributions of spatially averaged temperature (a) and relative humidity (b) in three representative zones over 60 days in 2024.

humidity distributions, together with CONUS-wide baselines, over 15 days in each month. The abnormally high contrail coverage in ZNY in July 2024 corresponds to concentrated low temperatures and humid air (middle column of Fig. 7), while partial high humidity in early October explains the enhanced contrails in ZMP. These results highlight the role of seasonal UTLS variability in contrail mitigation potential across regions.

2) Diurnal Patterns: Fig. 3 (a) shows that contrails occur more widely during the day than at night. Hourly contrail coverage over CONUS (Fig. 8) peaks at 0.164% around 10:00 and drops to 0.052% at 01:00, averaged over 60 days under

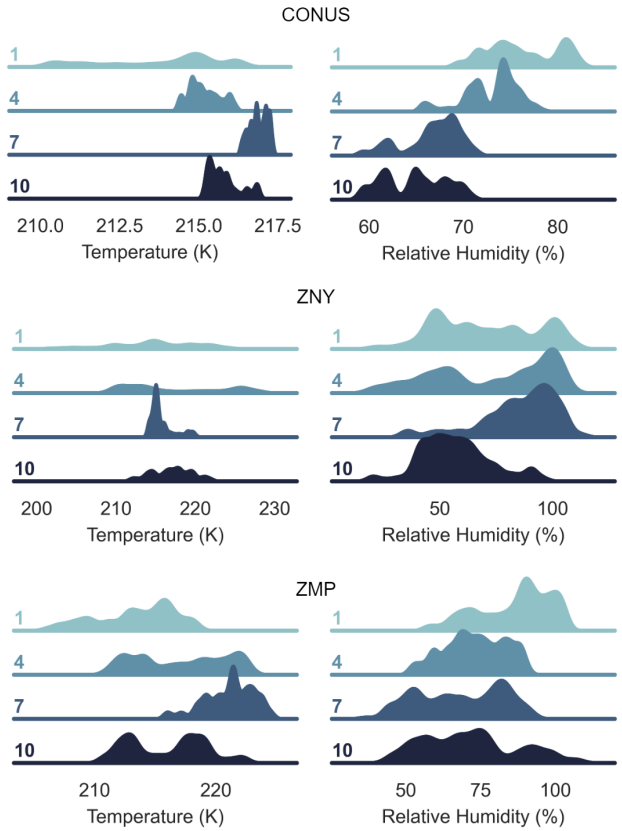

Figure 7. The spatially averaged temperature and relative humidity over months in CONUS, ZNY, and ZMP three regions.

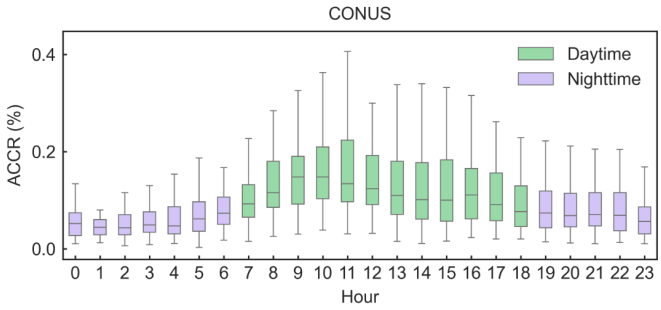

Figure 8. Hourly ACCR distribution over CONUS in CST time, averaged across 60 days in 2024.

the moderate estimate. This diurnal cycle, with a morning maximum and midnight minimum, is consistent with [18] and corroborated by our forthcoming 9-year analysis. Despite their smaller nighttime fraction, contrails exert disproportionately higher net radiative forcing as evaluated in [32].

V. Discussion

Although this study demonstrates the ability to estimate regional contrail coverage at high temporal resolution, the results remain influenced by moderate detection accuracy. False positives and missed detections propagate uncertainty into coverage estimates, potentially biasing climate assessments and misguiding rerouting strategies. This underscores the need for more abundant contrail labels and robust contrail segmentation, especially in challenging scenes, and for formal uncertainty quantification. Future work should integrate ensemble modelling and probabilistic detection to reduce uncertainty for strategic flight planning.

A further challenge is distinguishing contrails from visually overlapped natural cirrus. Our approach does not explicitly suppress cirrus contamination, risking underestimation in dense cloud regimes. Promising solutions include fusing satellite data with optical depth retrievals and cruise-level meteorological fields. Improved cross-sensor calibration could offer a better distinction of those aircraft-induced clouds.

Finally, this work evaluates only a single year. Extending the analysis across multiple years would allow assessment of intra-annual meteorological variability and improve the robustness of regional contrail climatology estimates.

VI. Conclusion

This work employs semantic segmentation to estimate contrail coverage at the ARTCC level across CONUS, relying on human-labelled contrail imagery learning. By exploiting the line-shaped structure of contrails, we proposed a joint spatial-frequency regularisation in model training, achieving consistent performance gains across metrics and thresholds. Multi-threshold analyses revealed close spatio-temporal patterns of contrail coverage, highlighting contrail-intense regions and corridors. While overall coverage agrees with prior studies, substantial variation across ARTCCs underscores the need for regionalised assessments. These insights can inform precise, region-specific flight planning targeting high-risk contrail zones.

A key direction for future work is to apply the proposed method to global satellite records for contrail lifetime estimation and climate forcing quantification. We will also develop refined rerouting strategies at regional and en-route levels, the feasibility and climate benefit of which will hinge on traffic density, airspace capacity, and contrail forecast quality.

Data Availability

The OpenContrails dataset was published by [1], and the labelling records are publicly available. Meteorological variables and air traffic flow data can be accessed from [21] and [23], respectively. Processed contrail imagery, detected contrail masks used for coverage estimation, are available from the corresponding author upon request.

Acknowledgment

The work reported in this paper was supported by grants from Research Grants Council, the Hong Kong Government (Grant No. PolyU15201423), Research Institute for Sustainable Urban Development (Grant No. BBG5), Department of Aeronautical and Aviation Engineering, The Hong Kong Polytechnic University, Hong Kong SAR (RMK1), and the National Natural Science Foundation of China (Grant No. 72301229).

REFERENCES

[1] J. Y.-H. Ng, K. McCloskey, J. Cui, V. R. Meijer, E. Brand, A. Sarna, N. Goyal, C. Van Arsdale, and S. Geraedts, "Contrail Detection on GOES-16 ABI With the OpenContrails Dataset," *IEEE Transactions on Geoscience and Remote Sensing*, vol. 62, pp. 1–14, 2024.

[2] M. Vázquez-Navarro, H. Mannstein, and S. Kox, "Contrail life cycle and properties from 1 year of MSG/SEVIRI rapid-scan images," *Atmospheric Chemistry and Physics*, vol. 15, no. 15, pp. 8739–8749, Aug. 2015.

[3] L. Dray, A. W. Schäfer, C. Grobler, C. Falter, F. Allroggen, M. E. J. Stettler, and S. R. H. Barrett, "Cost and emissions pathways towards net-zero climate impacts in aviation," *Nature Climate Change*, vol. 12, no. 10, pp. 956–962, Oct. 2022.

[4] R. Teoh, U. Schumann, A. Majumdar, and M. E. J. Stettler, "Mitigating the Climate Forcing of Aircraft Contrails by Small-Scale Diversions and Technology Adoption," *Environmental Science & Technology*, vol. 54, no. 5, pp. 2941–2950, Mar. 2020.

[5] A. Sonabend-W, C. Elkin, T. Dean, J. Dudley, N. Ali, J. Blickstein, E. Brand, B. Broshears, S. Chen, Z. Engberg, M. Galyen, S. Geraedts, N. Goyal, R. Grenham, U. Hager, D. Hecker, M. Jany, K. McCloskey, J. Ng, B. Norris, F. Opel, J. Rothenberg, T. Sankar, D. Sanekommu, A. Sarna, O. Schütt, M. Shapiro, R. Soh, C. Van Arsdale, and J. C. Platt, "Feasibility test of per-flight contrail avoidance in commercial aviation," *Communications Engineering*, vol. 3, no. 1, pp. 1–7, Dec. 2024.

[6] Z. L. Zengerling and A. Lau, "Reducing the Climate Impact of Flight Trajectories considering Network Effects," in *Proceedings of SESAR Innovation Days 2024*. Aeroporti di Roma, ENAV and Leonardo, p. 1. [Online]. Available: https://doi.org/10.61009/SID.2024.1.29

[7] M. J. Prather, A. Gettelman, and J. E. Penner, "Trade-offs in aviation impacts on climate favour non-CO2 mitigation," *Nature*, vol. 643, no. 8073, pp. 988–993, Jul. 2025.

[8] H. Appleman, "The Formation of Exhaust Condensation Trails by Jet Aircraft," *Bulletin of the American Meteorological Society*, vol. 34, no. 1, pp. 14–20, 1953.

[9] C. Akhtar Martínez, S. D. Eastham, and J. P. Jarrett, "Contrail models lacking post-fallstreak behavior could underpredict lifetime optical depth," pp. 1–26. [Online]. Available: https://egusphere.copernicus.org/preprints/2025/egusphere-2025-278/

[10] R. Teoh, U. Schumann, E. Gryspeerdt, M. Shapiro, J. Molloy, G. Koudis, C. Voigt, and M. E. J. Stettler, "Aviation contrail climate effects in the North Atlantic from 2016 to 2021," *Atmospheric Chemistry and Physics*, vol. 22, no. 16, pp. 10 919–10 935, Aug. 2022.

[11] R. Teoh, Z. Engberg, M. Shapiro, L. Dray, and M. E. J. Stettler, "The high-resolution Global Aviation emissions Inventory based on ADS-B (GAIA) for 2019–2021," *Atmospheric Chemistry and Physics*, vol. 24, no. 1, pp. 725–744, Jan. 2024.

[12] E. Roosenbrand, J. Sun, and J. Hoekstra, "Quantifying the efficacy of weather forecasting data for flight contrail optimization," in *Proceedings of SESAR Innovation Days 2024*. Rome, Italy: Aeroporti di Roma, ENAV and Leonardo, Dec. 2024.

[13] O. Ronneberger, P. Fischer, and T. Brox, "U-Net: Convolutional Networks for Biomedical Image Segmentation," in *Medical Image Computing and Computer-Assisted Intervention – MICCAI 2015*, N. Navab, J. Hornegger, W. M. Wells, and A. F. Frangi, Eds. Cham: Springer International Publishing, 2015, pp. 234–241.

[14] J. Ng, C. Elkin, A. Sarna, W. Reade, and M. Demkin, "Google research—identify contrails to reduce global warming. kaggle," 2023.

[15] F. Yin, V. Grewe, C. Frömming, and H. Yamashita, "Impact on flight trajectory characteristics when avoiding the formation of persistent contrails for transatlantic flights," *Transportation Research Part D: Transport and Environment*, vol. 65, pp. 466–484, Dec. 2018.

[16] A. Simorgh and M. Soler, "Climate-optimized flight planning can effectively reduce the environmental footprint of aviation in Europe at low operational costs," *Communications Earth & Environment*, vol. 6, no. 1, pp. 1–13, Jan. 2025.

[17] U. Schumann and K. Graf, "Aviation-induced cirrus and radiation changes at diurnal timescales," *Journal of Geophysical Research: Atmospheres*, vol. 118, no. 5, pp. 2404–2421, 2013.

[18] V. R. Meijer, L. Kulik, S. D. Eastham, F. Allroggen, R. L. Speth, S. Karaman, and S. R. H. Barrett, "Contrail coverage over the United States before and during the COVID-19 pandemic," *Environmental Research Letters*, vol. 17, no. 3, p. 034039, Mar. 2022.

[19] D. P. Duda, W. L. Smith Jr., S. Bedka, D. Spangenberg, T. Chee, and P. Minnis, "Impact of COVID-19-Related Air Traffic Reductions on the Coverage and Radiative Effects of Linear Persistent Contrails Over Conterminous United States and Surrounding Oceanic Routes," *Journal of Geophysical Research: Atmospheres*, vol. 128, no. 6, p. e2022JD037554, 2023.

[20] T. J. Schmit, S. S. Lindstrom, J. J. Gerth, and M. M. Gunshor, "Applications of the 16 spectral bands on the Advanced Baseline Imager (ABI)." *Journal of Operational Meteorology*, vol. 06, no. 04, pp. 33–46, Jun. 2018.

[21] B. Bell, H. Hersbach, A. Simmons, P. Berrisford, P. Dahlgren, A. Horányi, J. Muñoz-Sabater, J. Nicolas, R. Radu, D. Schepers, C. Soci, S. Villaume, J.-R. Bidlot, L. Haimberger, J. Woollen, C. Buontempo, and J.-N. Thépaut, "The ERA5 global reanalysis: Preliminary extension to 1950," *Quarterly Journal of the Royal Meteorological Society*, vol. 147, no. 741, pp. 4186–4227, Oct. 2021.

[22] M. Schäfer, M. Strohmeier, V. Lenders, I. Martinovic, and M. Wilhelm, "Bringing up OpenSky: A large-scale ADS-b sensor network for research," in *Proceedings of the 13th IEEE/ACM International Symposium on Information Processing in Sensor Networks (IPSN)*. IEEE, Apr. 2014, pp. 83–94.

[23] X. Olive, "Traffic, a toolbox for processing and analysing air traffic data," *Journal of Open Source Software*, vol. 4, p. 1518, 2019.

[24] Z. Tu, H. Talebi, H. Zhang, F. Yang, P. Milanfar, A. Bovik, and Y. Li, "MaxViT: Multi-axis Vision Transformer," in *Computer Vision – ECCV 2022*, S. Avidan, G. Brostow, M. Cissé, G. M. Farinella, and T. Hassner, Eds. Cham: Springer Nature Switzerland, 2022, pp. 459–479.

[25] G. Jarry, V. Torjman-Levavasseur, P. Very, and A. Heffar, "Deep semantic contrails segmentation of GOES-16 satellite images: A hyperparameter exploration," in *Proceedings of SESAR Innovation Days 2024*. Rome, Italy: Aeroporti di Roma, ENAV and Leonardo, Dec. 2024.

[26] R. Wightman, "Pytorch image models," https://github.com/rwightman/pytorch-image-models, 2019.

[27] I. Loshchilov and F. Hutter, "Decoupled Weight Decay Regularization," Jan. 2019.

[28] G. Dekoutsidis, H. Feidas, and L. Bugliaro, "Contrail detection on SEVIRI images and 1-year study of their physical properties and the atmospheric conditions favoring their formation over Europe," *Theoretical and Applied Climatology*, vol. 151, no. 3, pp. 1931–1948, Feb. 2023.

[29] P. Minnis, J. K. Ayers, M. L. Nordeen, and S. P. Weaver, "Contrail Frequency over the United States from Surface Observations," vol. 16, no. 21, pp. 3447–3462. [Online]. Available: http://journals.ametsoc.org/doi/10.1175/1520-0442(2003)016⟨3447:CFOTUS⟩2.0.CO;2

[30] U. Schumann, "A contrail cirrus prediction model," *Geoscientific Model Development*, vol. 5, no. 3, pp. 543–580, May 2012.

[31] R. Teoh, Z. Engberg, U. Schumann, C. Voigt, M. Shapiro, S. Rohs, and M. E. J. Stettler, "Global aviation contrail climate effects from 2019 to 2021," *Atmospheric Chemistry and Physics*, vol. 24, no. 10, pp. 6071–6093, May 2024.

[32] I. Ortiz, E. Dimitropoulou, P. de Buyl, N. Clerbaux, J. García-Heras, A. Jafarimoghaddam, H. Brenot, J. van Gent, K. Sievers, E. Otero, P. Loganathan, and M. Soler, "Satellite-based quantification of contrail radiative forcing over europe: A two-week analysis of aviation-induced climate effects," in *Proceedings of SESAR Innovation Days 2024*. Rome, Italy: Aeroporti di Roma, ENAV and Leonardo, Dec. 2024.